Bulletin of the Seismological Society of America, Vol. 95, No. 3, pp. 1170–1180, June 2005, doi: 10.1785/0120040094

Finite-Moment Tensor of the 3 September 2002 Yorba Linda Earthquake

by Po Chen, Thomas H. Jordan, and Li Zhao

Abstract We have developed procedures for inverting broadband waveforms for the finite-moment tensors (FMTs) of regional earthquakes. The FMT is defined in terms of second-order polynomial moments of the source space–time function; it removes the fault-plane ambiguity of the centroid moment tensor (CMT) and yields several additional parameters of seismological interest: the characteristic length L_c, width W_c, and duration T_c of the faulting, as well as the directivity vector $\mathbf{v}_d$ of the fault slip. Following McGuire *et al.* (2001), we represent the observed waveform relative to the synthetic in terms of two frequency-dependent differential times, a phase delay $\delta\tau_p(\omega)$ and an amplitude-reduction time $\delta\tau_q(\omega)$, which we measure using the generalized seismological data functional (GSDF) method (Gee and Jordan, 1992). We numerically calculate the FMT partial derivatives, which allows us to use synthetics computed by using any forward-modeling tools. We have tested our methodology on Southern California Seismic Network (SCSN) recordings of the 03 September 2002 Yorba Linda earthquake (M_W 4.3). Using 1D synthetic Green's functions, we determined the CMT and resolved fault-plane ambiguity. To resolve the details of source finiteness, we employed a joint-inversion technique that recovers the CMT parameters of the aftershocks and the CMT and FMT parameters of the mainshock. The joint system of equations relating the data to the source parameters of the mainshock–aftershock cluster is denuisanced for path anomalies in both observables; this projection operation effectively corrects the mainshock data for path-related anomalies in a way similar to, but more flexible than, empirical Green's function (EGF) techniques. Our results indicate that the Yorba Linda rupture occurred as left-lateral slip on a fault-patch conjugate to the nearby, right-lateral Whittier fault. We obtained source dimensions of $L_c = 0.7 \pm 0.1$ km, $W_c = 0.4 \pm 0.1$ km, and $T_c = 0.2 \pm 0.05$ sec, implying a stress drop of about 3.2 MPa, and we found a directivity of 0.8 ± 0.2, oriented up and to the northeast. The inferred fault plane is consistent with the mainshock–aftershock distribution relocated by Hauksson *et al.* (2002).

Introduction

Seismic-hazard analysis depends on seismology to quantify earthquake sources. Although any indigenous seismic source can be exactly represented by a space–time distribution of stress glut $\Gamma(\mathbf{r}, t)$ (Backus and Mulcahy, 1976), this general representation is rarely used. Instead, seismologists approximate $\Gamma(\mathbf{r}, t)$ in various ways, depending on the observational circumstances. Three representations are commonly employed in Southern California, which is our primary area of interest (Fig. 1):

1. Isotropic point source (IPS), specified by an origin time t_0, a hypocenter $\mathbf{r}_0$, and local magnitude M_L. The Southern California Seismic Network (SCSN) routinely recovers and catalogs the IPS representation for events as small as $M_L \approx 1.0$–1.5 (Mori *et al.*, 1998).
2. Centroid moment tensor (CMT), specified by a symmetric seismic-moment tensor $\mathbf{M}$, a centroid time t_1, and a centroid location $\mathbf{r}_1$ (Dziewonski *et al.*, 1981). The ten-parameter CMT representation is the most general indigenous point source, although supplementary restrictions are often applied to reduce the parameter set; for example, only eight parameters are needed to describe a pure double couple. Source mechanisms are regularly determined from SCSN first motions down to $M_L \approx 2.0$–2.5 (Hauksson, 2000), and complete CMT solutions can be automatically recovered from broadband waveform data for $M_L > 3.0$–3.5 (Zhu and Helmberger, 1996; Pasyanos *et al.*, 1996).
3. Fault-slip distribution (FSD), specified by a displacement discontinuity $\Delta\mathbf{u}(\mathbf{r}, t)$ across a predetermined fault plane $\mathbf{r} \in S$. Depending on the parameterization and kinematic

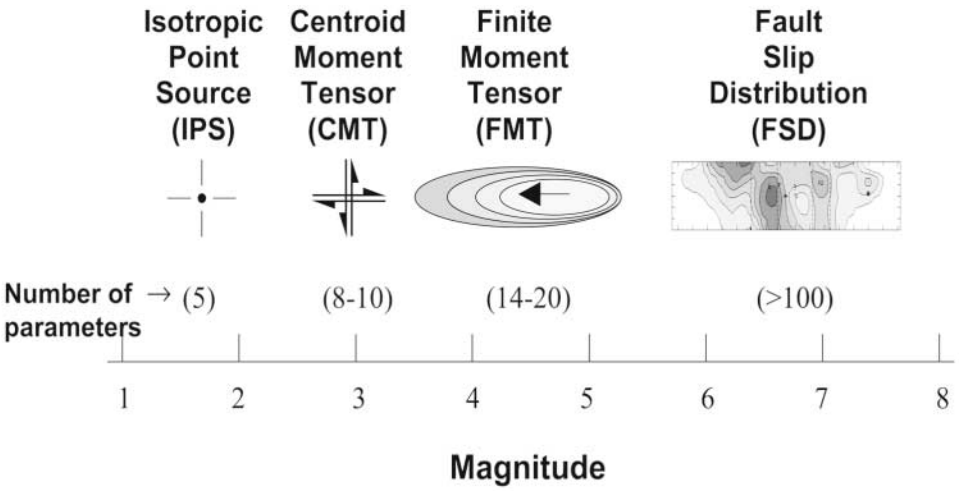

Figure 1. Four source representations discussed in the text, arrayed near the lower end of the magnitude range of their applicability in Southern California. We have developed the methodology for recovering FMT representations of earthquakes in the magnitude range 4–6 from regional broadband data. The number of FMT parameters varies from 14 to 20, depending on the constraints on the source model.

assumptions, the number of unknown parameters can easily exceed 100. Full FSD imaging is usually applied only to large (M_L >6) earthquakes, such as the 1992 Landers earthquake (Cohee and Beroza, 1994; Wald and Heaton, 1994), the 1994 Northridge earthquake (Wald *et al.*, 1996), and the 1999 Hector Mine earthquake (Dreger and Kaverina, 2000).

In this article, we discuss new procedures for determining source parameters by using a "finite-moment tensor" (FMT), the lowest-order representation of a finite fault. The FMT resolves fault-plane ambiguity of the CMT and provides several additional parameters of seismological interest, including the characteristic length L_c, width W_c, and duration T_c of the faulting, as well as the directivity vector $\mathbf{v}_d$ of the fault slip. We expect the FMT representation to be most useful for earthquakes in the magnitude range $M_L \approx 4$–6, where finite-source effects can be resolved from regional broadband data but are too small to warrant a full FSD analysis (Fig. 1).

We have successfully applied our method to recover the FMT for 3 September 2002 Yorba Linda earthquake (M_L 4.8) using high-quality waveform data from the TriNet seismic network (Hauksson *et al.*, 2001). The 24 broadband stations used in this study are shown on Figure 2, and some examples of recorded and synthetic seismograms are shown on Figure 3.

The Finite-Moment Tensor

Our formulation of the FMT representation follows McGuire *et al.* (2001) in assuming the stress glut is everywhere proportional to a constant seismic-moment tensor,

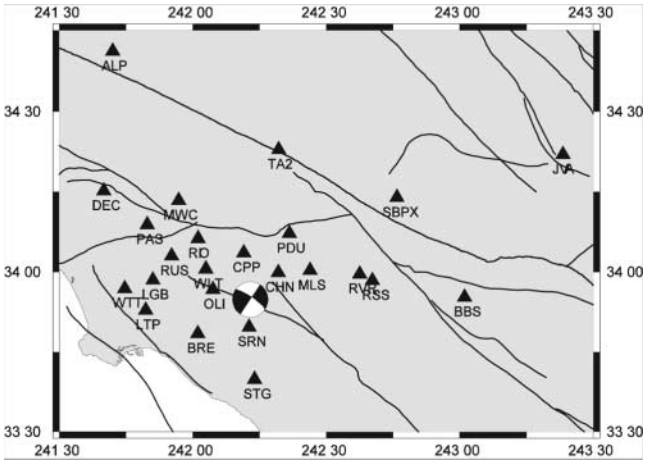

Figure 2. The beachball shows the location and focal mechanism of the Yorba Linda earthquake determined by us using 1D synthetic Green's functions. The 24 TriNet stations used in this study are shown as triangles. Major faults in this region are shown as solid lines.

$$\Gamma(\mathbf{r},t) = \mathbf{M} \int_{t_0}^{t} f(\mathbf{r},t')dt'. \quad (1)$$

The excitation of seismic waves is thus proportional to the source space–time function $f(\mathbf{r}, t)$, which we assume is zero before an origin time t_0. We expand $f(\mathbf{r}, t)$ in terms of its space–time polynomial moments $\boldsymbol{\mu}^{(m,l)}$ (Backus and Mulcahy, 1976) and approximate it by the low-order terms. The zeroth-order moment is unity by definition, $\mu^{(0,0)} = \iint f(\mathbf{r}, t)\, dV\, dt = 1$, and the first-order moments provide the spatial and temporal centroids:

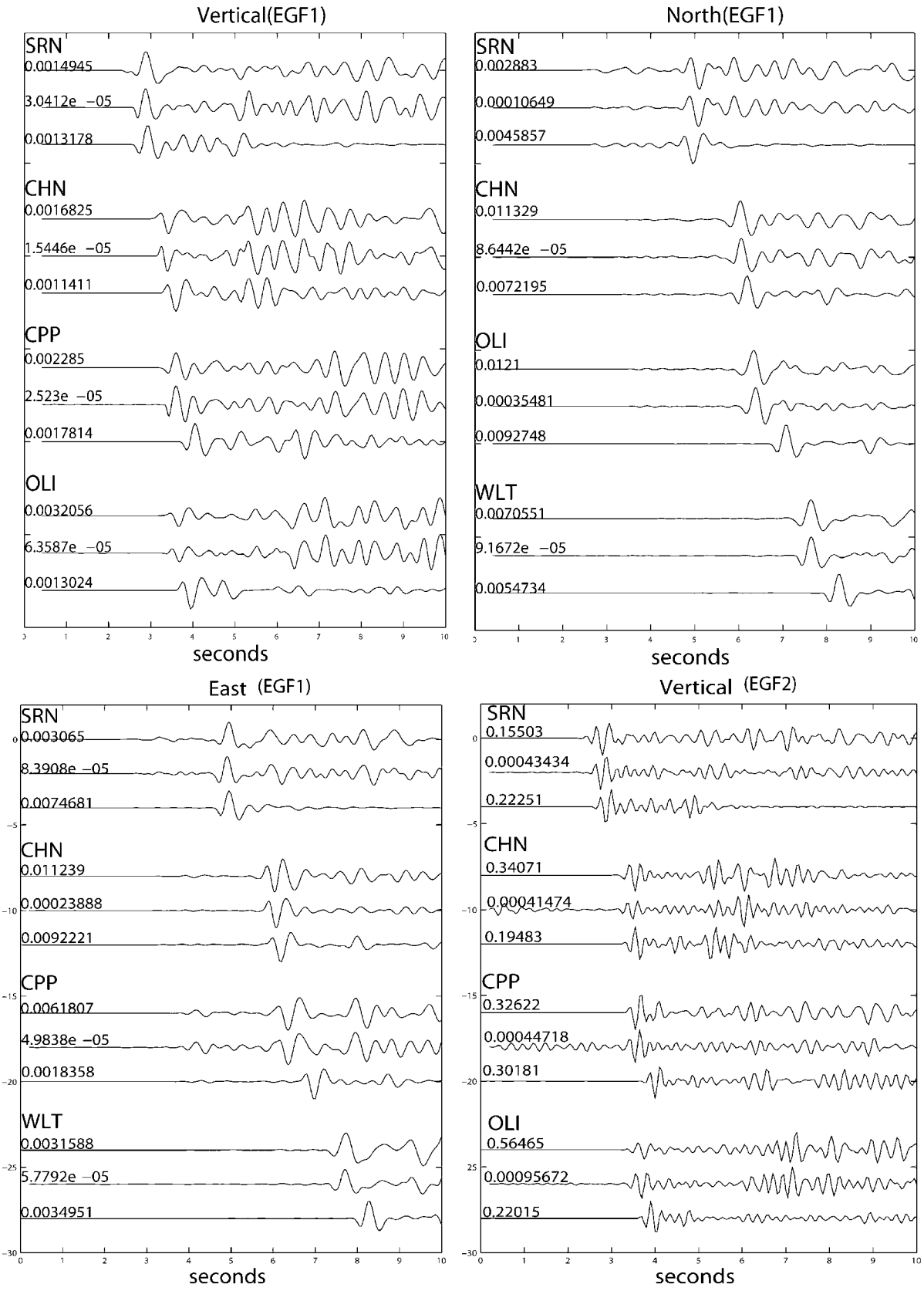

Figure 3. Some examples of recorded and synthetic seismograms show *P* waves on vertical components and *S* waves on east and north components. Seismograms on Vertical (EGF1), North (EGF1), and East (EGF1) are bandpass filtered from 0.5 Hz to 2.5 Hz; seismograms on Vertical (EGF2) are bandpass filtered from 1.5 Hz to 5 Hz. Upper trace, mainshock; middle trace, one of the aftershocks used in our study; lower trace, synthetic Green's function. Numbers show the peak amplitudes in centimeters per second. In our FMT inversions, we assume the aftershocks have the same focal mechanism as the mainshock, consistent with the data shown here.

$$\boldsymbol{\mu}^{(1,0)} = \iint f(\mathbf{r},t)\mathbf{r}dV\,dt \equiv \mathbf{r}_1, \tag{2a}$$

$$\mu^{(0,1)} = \iint f(\mathbf{r},t)t dV\,dt \equiv t_1. \tag{2b}$$

The tensor $\mathbf{M}$, vector $\mathbf{r}_1$, and scalar t_1 form the CMT (point-source) representation.

The lowest-order description of source finiteness is given by the second moments. The second central moment in time specifies the characteristic duration of the event (Silver and Jordan, 1983),

$$\hat{\mu}^{(0,2)} = \iint f(\mathbf{r},t)(t - t_1)^2\,dV\,dt \equiv (T_c/2)^2. \tag{3}$$

The second central moment in space is a symmetric second-order tensor,

$$\hat{\boldsymbol{\mu}}^{(2,0)} = \iint f(\mathbf{r},t)(\mathbf{r}-\mathbf{r}_1)(\mathbf{r}-\mathbf{r}_1)^T dV\,dt = \mathbf{U}\boldsymbol{\Lambda}\mathbf{U}^T. \tag{4}$$

Here, $\boldsymbol{\Lambda}$ is a diagonal matrix of eigenvalues, and $\mathbf{U}$ is an orthogonal matrix of eigenvectors. For the special case of a planar rectangular dislocation of length L and width W, the eigenvalue matrix reduces to

$$\boldsymbol{\Lambda} = \mathrm{diag}[(L_c/2)^2, (W_c/2)^2, 0], \tag{5}$$

where $L_c = L/\sqrt{3}$ is the characteristic length and $W_c = W/\sqrt{3}$ is the characteristic width of the source. The mixed space–time moment gives the directivity vector (Ben-Menahem, 1961):

$$\hat{\boldsymbol{\mu}}^{(1,1)} = \iint f(\mathbf{r},t)(\mathbf{r}-\mathbf{r}_1)(t-t_1)dV\,dt \equiv \hat{\mu}^{(0,2)}\,\mathbf{v}_d. \tag{6}$$

The directivity velocity vector $\mathbf{v}_d$ will lie in the plane of a simple dislocation. The magnitude of this vector is zero for a symmetric bilateral rupture and L_c/T_c for a unilateral rupture along the length of the fault. Hence, the ratio $d \equiv \|\mathbf{v}_d\| T_c/L_c$ measures the magnitude of the directivity as a dimensionless number between zero and unity (McGuire *et al.*, 2002).

Under the strictures of equation (1), the FMT representation comprises 20 parameters, 10 for the CMT plus 10 for the second central moments of $f(\mathbf{r}, t)$. For most small and many moderate earthquakes, a planar dislocation may provide an adequate source model, in which case the total number of FMT parameters reduces to 14: eight CMT parameters plus L_c, W_c, T_c, d, one principal-axis orientation parameter in $\mathbf{U}$, and one vector orientation parameter in $\mathbf{v}_d$.

To recover FMTs for moderate earthquakes by using regional networks, we must correct the waveforms for propagation effects, which in Southern California can be strongly 3D. Most previous researchers have accounted for the inadequacy of available Earth models by using empirical Green's functions (EGFs). One EGF method is to deconvolve the propagation effects by using the waveforms from proximate events of negligible spatial and temporal extent, such as small aftershocks, and then invert the pulses resulting from deconvolution for a slip distribution (Mori and Hartzell, 1990; Mori, 1996; Courboulex *et al.*, 1998). McGuire's (2004) recent study of small earthquakes shows that this type of EGF analysis can also give robust estimates of FMT parameters. A more direct EGF method is to match the mainshock waveforms by superposing EGFs constrained by kinematic rupture models, thus avoiding deconvolution (Hellweg and Boatwright, 1999; Okada *et al.*, 2001).

Our objective is to develop a methodology for FMT inversion that does not rely on deconvolution and can take full advantage of model-based Green's functions—synthetic seismograms—as well as EGFs. In this preliminary study, we have used synthetics from 1D structural models, but our formulation can be easily adapted to 3D structures now available for Southern California, such as the Southern California Earthquake Center (SCEC) Community Velocity Model (Magistrale *et al.*, 2000; Hauksson, 2000; Kohler *et al.*, 2003) and the Harvard Model (Süss and Shaw, 2003; Komatitsch *et al.*, 2004). Our procedure requires the computation of synthetic seismograms and partial derivatives to set up the inversion, which can be avoided in traditional EGF analysis, but it pays off by allowing us to incorporate more information about Earth structure and the distribution of seismic sources in the determination of the FMT. Moreover, it provides a uniform methodology to invert waveforms for both Earth and source structure.

Generalized Seismological Data Functional (GSDF) Analysis

In the frequency domain, an observed waveform $u(\mathbf{r}_R, \omega)$ at a receiver location $\mathbf{r}_R$ can be related to a point-source synthetic waveform $\tilde{u}(\mathbf{r}_R, \omega)$ by a differential operator expressed in the exponential (Rytov) form:

$$u(\mathbf{r}_R,\omega) = \tilde{u}(\mathbf{r}_R,\omega)\,\exp^{[i\omega\delta\tau_p(\omega)-\omega\delta\tau_q(\omega)]}, \tag{7}$$

where $\delta\tau_p(\omega)$ is a frequency-dependent phase-delay time, and $\delta\tau_q(\omega)$ is an "amplitude-reduction" time, so named because a positive value of $\delta\tau_q$ reduces the amplitude of u relative to $\tilde{u}$. McGuire *et al.* (2001) have linearized the forward problem of relating the functionals $\delta\tau_{p,q}$ to the FMT parameters $\boldsymbol{\mu}^{(m,l)}$ to obtain:

$$\delta\tau_q^n(\mathbf{r}_R,\omega) = \boldsymbol{\mu}^{(1,0)} \cdot \nabla_S \tilde{\tau}_q^n + \frac{\omega}{2}\mu^{(0,2)} + \omega\boldsymbol{\mu}^{(1,1)} \cdot \nabla_S \tilde{\tau}_p^n + \frac{1}{2}\boldsymbol{\mu}^{(2,0)} : \tilde{\mathbf{X}}_n, \tag{8a}$$

$$\delta\tau_p^n(\mathbf{r}_R,\omega) = \mu^{(0,1)} + \boldsymbol{\mu}^{(1,0)} \cdot \nabla_S \tilde{\tau}_p^n + \omega\boldsymbol{\mu}^{(1,1)} \cdot \nabla_S \tilde{\tau}_q^n + \frac{1}{2}\boldsymbol{\mu}^{(2,0)} : \tilde{\mathbf{Y}}_n, \tag{8b}$$

Here ∇_S is the gradient operator with respect to the source coordinates, and the second-order spatial derivatives are

$$\tilde{\mathbf{X}}_n = \nabla_S \nabla_S \tilde{\tau}_q^n + \omega \nabla_S \tilde{\tau}_p^n \nabla_S \tilde{\tau}_p^n - \omega \nabla_S \tilde{\tau}_q^n \nabla_S \tilde{\tau}_q^n, \quad (9a)$$

$$\tilde{\mathbf{Y}}_n = \nabla_S \nabla_S \tilde{\tau}_p^n - \omega \nabla_S \tilde{\tau}_q^n \nabla_S \tilde{\tau}_q^n - \omega \nabla_S \tilde{\tau}_p^n \nabla_S \tilde{\tau}_p^n, \quad (9b)$$

We computed the first- and second-order spatial derivatives by applying a symmetrized finite-difference formula (Press *et al.*, 2001) to point-source synthetic seismograms, which were calculated for 1D, multilayered velocity models by using Zhu and Rivera's (2002) frequency-wavenumber method.

Examples of the partial derivatives of $\delta\tau_q$ with respect to the source parameters (sensitivity coefficients) are shown for *P* waves from the Yorba Linda earthquake in Figure 4. Some intuitive aspects can be seen; for example, the sensitivity coefficients for directivity parameters increase with frequency and are negative in the direction of rupture propagation, because a negative $\delta\tau_q$ implies an amplitude increase. The kernel for second-order spatial moment has a cos 2θ dependence on the azimuth because of constructive and destructive interference from waves generated by a finite source. For more examples of $\delta\tau_{p,q}$ sensitivity coefficients, we refer to McGuire *et al.* (2001).

The phase-delay times and amplitude-reduction times were measured by using Gee and Jordan's (1992) method of GSDF, as illustrated in Figure 5. In the GSDF analysis, the targeted wave group, a body wave, surface wave, or any other phase, is computed for a point-source model, and this "isolation filter" is cross-correlated both with the observed seismogram and with the full synthetic seismogram. The resulting cross-correlograms are windowed in a time domain in the vicinity of their peaks and narrowband filtered at a target frequency ω_i. The resulting waveforms can be approximated by Gaussian wavelets, and the parameters of these wavelets can be used to recover estimates of $\delta\tau_p(\omega_i)$ and $\delta\tau_q(\omega_i)$ corrected for filtering bias and interference effects (Gee and Jordan, 1992; Chen *et al.*, 2003).

The GSDF methodology provides a unified approach to the analysis and interpretation of the information on seismograms. It can be applied to any waveform on any component and, through the use of synthetic seismograms, can incorporate existing knowledge of source and Earth structure. The processing algorithm can use synthetic waveforms from 1D or 3D models as isolation filters and accounts for waveform interference, *P-SV* coupling, and other complications modeled by the synthetics. Moreover, the algorithm automatically encodes the metadata needed for computing the Fréchet kernels that specify the sensitivity of the phase and amplitude data to lateral and radial Earth structure (Zhao and Jordan, 1998; Zhao *et al.*, 2000). The regional waveform data measured by this technique can therefore be used in joint inversions for source and Earth structure, including the evaluation and improvement of 3D regional Earth models (Chen *et al.*, 2003).

Single-Event Inversion

The linearized forward problem described by equations (8a) and (8b) can be written in the form

$$\mathbf{A}_0\mathbf{m}_0 + \mathbf{A}_1\mathbf{m}_1 + \mathbf{A}_2\mathbf{m}_2 = \mathbf{d}. \quad (10)$$

Here $\mathbf{d}$ is a data vector of GSDF measurements of $\delta\tau_p$ and $\delta\tau_q$ relative to the point-source synthetic seismograms, and the integer subscripts on the model vectors $\mathbf{m}_k$ denote the polynomial order of the source moment; that is, the vector $\mathbf{m}_0$ contains the perturbations to the zeroth moment (the moment tensor), $\mathbf{m}_1$ specifies the centroid space and time shifts $[\boldsymbol{\mu}^{(1,0)}, \mu^{(0,1)}]$, $\mathbf{m}_2$ comprises the second-order moments $[\boldsymbol{\mu}^{(2,0)}, \boldsymbol{\mu}^{(1,1)}, \mu^{(0,2)}]$, and the matrices $\mathbf{A}_k$ contain the partial derivatives (sensitivity coefficients) of the data with respect to the model parameters. We note that the relative magnitudes of the sensitivity coefficients for $\delta\tau_p$ and $\delta\tau_q$ alternate with the order number k; the $\delta\tau_q$ coefficients are generally larger for k even, whereas the $\delta\tau_p$ coefficients are larger for k odd.

The geologic structure of the upper crust in Southern California is known to be very heterogeneous laterally and vertically. To account for the grosser aspects of the geographic heterogeneity, we extracted path-specific 1D velocity structures from Version 3.0 of the 3D SCEC Community Velocity Model (Hauksson, 2000; Magistrale *et al.*, 2000; Kohler *et al.*, 2003) by horizontally averaging wave slownesses along source-receiver paths. We refer to these path-dependent 1D structures collectively as the A1D model.

The data were inverted using a hierarchical, iterative method that began with observations at lower frequencies. We low-pass filtered both the recorded seismograms and the point-source synthetics from the A1D model below 0.2 Hz and made GSDF measurements on 48 waveforms of *P*, *S*, and surface waves from TriNet records with good azimuthal distribution (Fig. 2). The process was initiated by inverting the low-frequency measurements of the amplitude reduction times $\delta\tau_q$ for an improvement to the moment tensor $\mathbf{M}$. We obtained a static moment of 3.5×10^{15} N m (M_w 4.3) and the double-couple solution shown in Figure 2. The latter was in good agreement with the SCSN focal mechanism determined from first-motion data (Hauksson *et al.*, 2002). Our best estimate of $\mathbf{M}$ had a small non-double-couple component, but a bootstrap test showed that the deviation from a pure double couple was statistically insignificant.

In the next step, we inverted the phase delays $\delta\tau_p$ for improvements to the source centroid. The spatial centroid shifted by only 0.2 km from the original SCSN location, which we again found to be statistically insignificant. Finally, we inverted the low-frequency amplitude data for the second-order moments to obtain the full FMT. The solution yielded a northeast-striking fault plane with a characteristic duration of about 0.1–0.2 sec and a characteristic dimension of 1–2 km. The bootstrap test identified the northeast nodal plane as the fault plane with reasonably high (81%) confi-

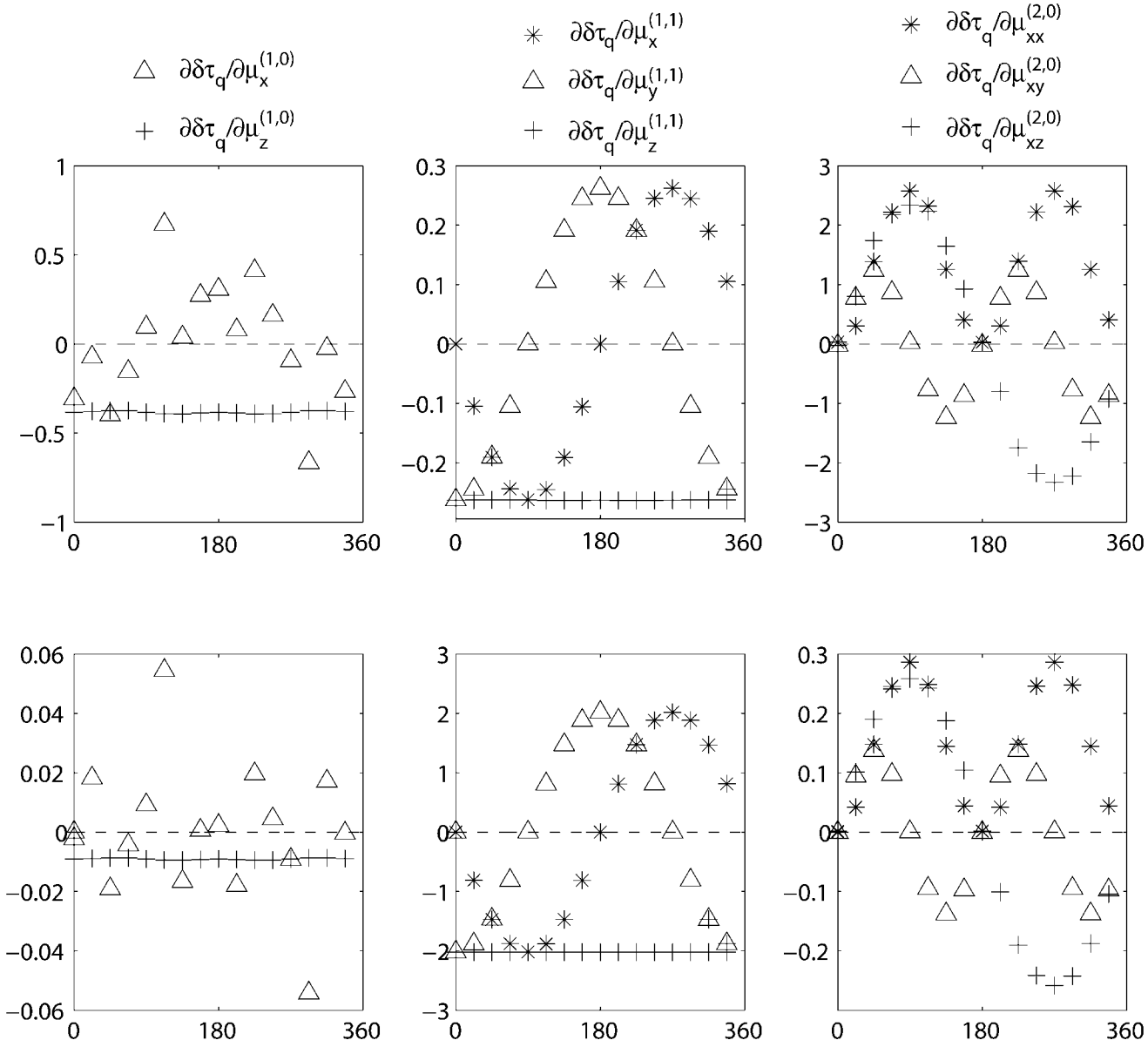

Figure 4. Plots of the sensitivity coefficients for $\delta\tau_q$ as a function of azimuth for *P* waves from the Yorba Linda earthquake. Left column, coefficients for a centroid shift (triangles, derivative relative to a perturbation toward north; pluses, a perturbation upward). Center column, coefficients for the directivity moment $\boldsymbol{\mu}^{(1,1)}$ (triangles, rupture propagates toward north; asterisks, rupture propagates toward east; pluses, rupture propagates upward). Right column, coefficients for second-order spatial moment $\boldsymbol{\mu}^{(2,0)}$ (asterisks, $\mu_{xx}^{(2,0)}$; triangles, $\mu_{xy}^{(2,0)}$; pluses, $\mu_{xz}^{(2,0)}$). Upper row, 0.2 Hz; lower row, 2.0 Hz. Dashed lines indicate zero. The sensitivity of $\delta\tau_q$ with respect to directivity increases with frequency, whereas the sensitivity to centroid shift and second-order spatial moment decreases with frequency. The apparent scatter in the first column is caused by singularities at 30°, 120°, 210°, and 300° azimuth, which are the nodal planes of *P*-wave radiation pattern.

dence, but we found that the uncertainties in L_c were comparable with its magnitude and that the low-frequency data placed no useful constraints on the directivity vector $\mathbf{v}_d$. Using higher-frequency data did not improve the solution.

Our results show that at low frequencies, where directivity caused by $\boldsymbol{\mu}^{(1,1)}$ has only a small effect, it is still possible to resolve fault-plane ambiguity by careful analysis of the constructive and destructive interference effects caused by source finiteness $\boldsymbol{\mu}^{(2,0)}$, whose relative contribution to amplitude-reduction time $\delta\tau_q$ is larger at a lower frequency (Fig. 4). For a pure bilateral rupture with a strike of 30°, the amplitude of finite-source waveform relative to the point-source

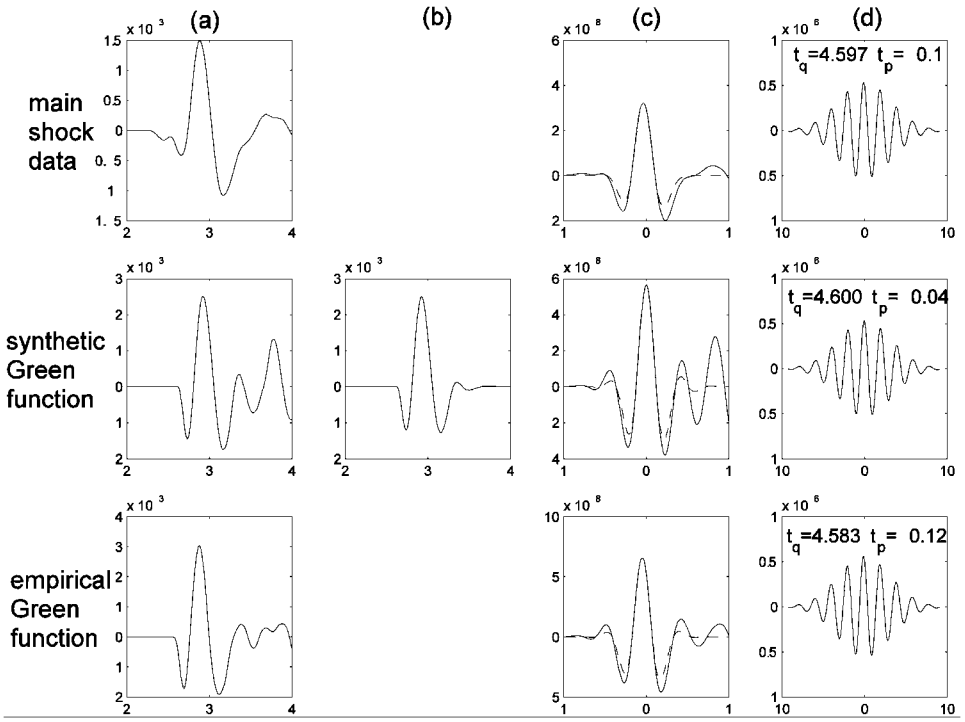

Figure 5. Examples of GSDF processing. (a) Observed and synthetic seismograms. (b) The isolation filter shown was obtained by windowing the full synthetic. (c) The cross-correlograms shown were windowed (dashed lines) and narrowband filtered. (d) The resulting waveforms shown can be approximated by Gaussian wavelets parameterized by t_q and t_p. The differential measurements of $\delta\tau_{p,q}$ are then recovered from these parameters.

synthetic waveform should be maximized at azimuths of 120° and 300°, owing to constructive interference, whereas slip on the conjugate fault plane would generate a maximum at 30° and 210°. At frequencies below 0.2 Hz, the synthetic Green's functions computed using path-specific 1D structure models are good enough to detect such interference effects.

In most previous studies, the fault planes of smaller earthquakes have been identified from directivity effects in the amplitudes and the widths of EGF-deconvolved source pulses (Mori and Hartzell, 1990; Mori, 1996). Our results are similar to those of McGuire (2004), who showed that the fault-plane ambiguity can be resolved by using EGF-derived estimates of $\mu_s^{(0,2)}$ even if the directivity is small. Our approach has the advantage of being applicable to events lacking suitable EGFs.

Multiple-Event Inversion

FMT estimation uncertainties for the single-event inversion are dominated by signal-generated noise. The finite-source perturbations to the GSDF observations for an event as small as the Yorba Linda earthquake are less than about 0.3 sec. Chen *et al.* (2003) have shown that, relative to A1D synthetics, lateral heterogeneity in Southern California introduces fluctuations in $\delta\tau_q$ that have a root-mean-square (rms) magnitude of about 0.45 sec for *P* and *S* phases in the frequency band of 0.2–1.2 Hz. This scatter can be reduced by using SCEC CVM3.0 to generate the reference seismograms, but the rms residuals are still on the order of 0.35 sec (Chen *et al.*, 2003), larger than the finite-source signal.

To improve the signal-to-noise ratio, we formulated a joint-inversion procedure that recovers the CMT parameters of the aftershocks and the FMT parameters of the mainshock. For each event in the cluster ($j = 1$ for the mainshock; $j = 2, 3, \ldots$, for aftershocks), we write the linearized perturbation equation:

$$\mathbf{A}_0^j \mathbf{m}_0^j + \mathbf{A}_1^j \mathbf{m}_1^j + \mathbf{A}_2^j \mathbf{m}_2^j = \mathbf{B}^j \mathbf{n} = \mathbf{d}^j. \quad (11)$$

The vector $\mathbf{n}$ is a set of path anomalies, which we treat as nuisance parameters. We assumed the dimensions of the cluster are small compared with the path lengths and, therefore, $\mathbf{n}$ is approximately the same for all events in a cluster. Because the aftershocks were small, we further assumed the effects of source finiteness were negligible; that is, $\mathbf{m}_2^j = 0$ for $j = 2, 3, \ldots$

With these assumptions, the path anomalies can be effectively removed by applying a projection operator that annihilates the terms $\mathbf{B}^j \mathbf{n}$ in (11). Let $\mathbf{A}_k$, $\mathbf{B}_k$, and $\mathbf{d}$ be the concatenations of $\{\mathbf{A}_k^j\}$, $\{\mathbf{B}_k^j\}$, and $\{\mathbf{d}^j\}$ for $k = 0$, 1, 2 and

$j = 0, 1, 2, 3, \ldots$. Then, the appropriate annihilator is $\mathbf{Q_B} = \mathbf{I} - \mathbf{B}(\mathbf{B}^T\mathbf{B})^{-1}\mathbf{B}^T$, and the reduced system of equations can be written in the form

$$\mathbf{Q_B A_0 m_0} + \mathbf{Q_B A_1 m_1} + \mathbf{Q_B A_2 m_2} = \mathbf{Q_B d}. \quad (12)$$

This type of "denuisancing" procedure has been commonly used in relative-location techniques (Jordan and Sverdrup, 1981). When observations are available for all events from all stations in the network, the $\mathbf{B}^j$ matrices are simply identity matrices; then, under our assumptions, $\mathbf{Q_B A_2} = \mathbf{A_2}$, and the projected data for the mainshock are equal to the original data, $\mathbf{d}^0$, corrected for path anomalies by subtracting the average value of the aftershock data. When some stations do not provide data for all events, the results are optimal in a least-squares sense (Jordan and Sverdrup, 1981).

The multiple-event method is closely related to traditional EGF analysis, but it offers several advantages. No waveform deconvolution is involved, and it can utilize data from more than one aftershock, including aftershocks recorded by only a subset of stations, allowing better averaging in the removal of the path anomalies. Moreover, because the perturbations are computed relative to synthetic seismograms, our methods can utilize the information in 3D seismic-velocity models.

Results

More than 50 Yorba Linda aftershocks with local magnitudes ranging from 0.9 to 3.0 were located by the SCSN. For this preliminary multiple-event inversion, we selected a M_L 2.9 aftershock that occurred 7 min after the mainshock (07:15:51.26 UTC) and a M_L 2.0 aftershock 4 min after the mainshock (07:12:55.20 UTC); these were designated EGF1 and EGF2, respectively. We measured the amplitude-reduction times $\delta\tau_q$ on 28 *P* waves and 28 *S* waves at frequencies ranging from 0.5 Hz to 2.5 Hz.

Based on relocations by E. Hauksson (personal comm. 2002), the distances between mainshock and aftershock hypocenters are 0.2 km for EGF1 and 0.4 km for EGF2. A comparison of the three events across their common band of observation showed that Hauksson's relative location was good and that the moment tensors of both the mainshock and the two aftershocks were well described by the same focal mechanism. We therefore approximated the aftershocks as point sources with our low-frequency mechanism (Fig. 2). The differences in scalar moment between the mainshock and the two aftershocks can be denuisanced by normalizing mainshock and aftershock data to the same scalar moment. The amplitude-reduction times used in this study were insensitive to the relative distances between mainshock and aftershock centroid location, so we dropped the first two terms in equation (12). The effects of denuisancing on the frequency-dependent data from two of the stations are shown in Figure 6.

To solve the inverse problem, we used a semidefinite programming method (Vandenberghe and Boyd, 1996), which fits the data by least-squares while incorporating various nonlinear constraints, such as the positivity of the space–time source ellipsoid (McGuire *et al.*, 2001). The inversion results are given in Table 1 and Figure 8, and the fit to the observations is presented in Figure 7. With the source ellipsoid $\boldsymbol{\mu}^{(2,0)}$ unconstrained in orientation, the inversion resolved the fault-plane ambiguity at a very high confidence level (>99%). In the optimized solution, the source directivity points to the northeast and slightly upward, consistent with the source ellipsoid principal axes.

Hence, the multiple-event inversion confirms that the Yorba Linda earthquake involved a left-lateral rupture on a plane conjugate to the nearby right-lateral Whittier fault (Fig. 8). This conclusion is consistent with the aftershock distribution relocated by E. Hauksson (personal comm.,

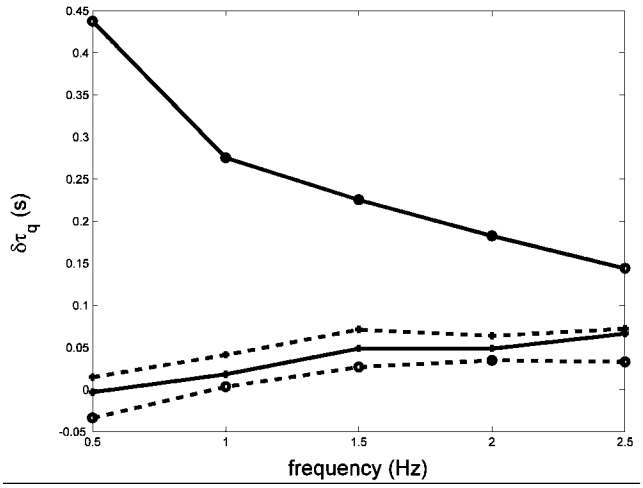

Figure 6. Measurements of $\delta\tau_q$ for *P* waves on the vertical component of station SRN (pluses) and MWC (filled circles). Solid line, raw observations; dashed line, denuisanced for path effects by using the aftershock data.

Table 1
Inverted FMT Parameters for 3 September 2002 Yorba Linda Earthquake

Parameters	Without Constraints*	With Constraints†
L_c (km)	1.47	0.74
W_c (km)	0.64	0.40
T_c (sec)	0.15	0.19
d	0.39	0.80
Strike (°)	39.8	33.2
Dip (°)	83.2	88.3
Stress drop (bars)	4	32
Rupture velocity (km/sec)	6.1	3.2

*Results obtained without any constraints except the positivity of source space–time volume.

†Results obtained by constraining the rupture velocity below shear-wave velocity in the inversion.

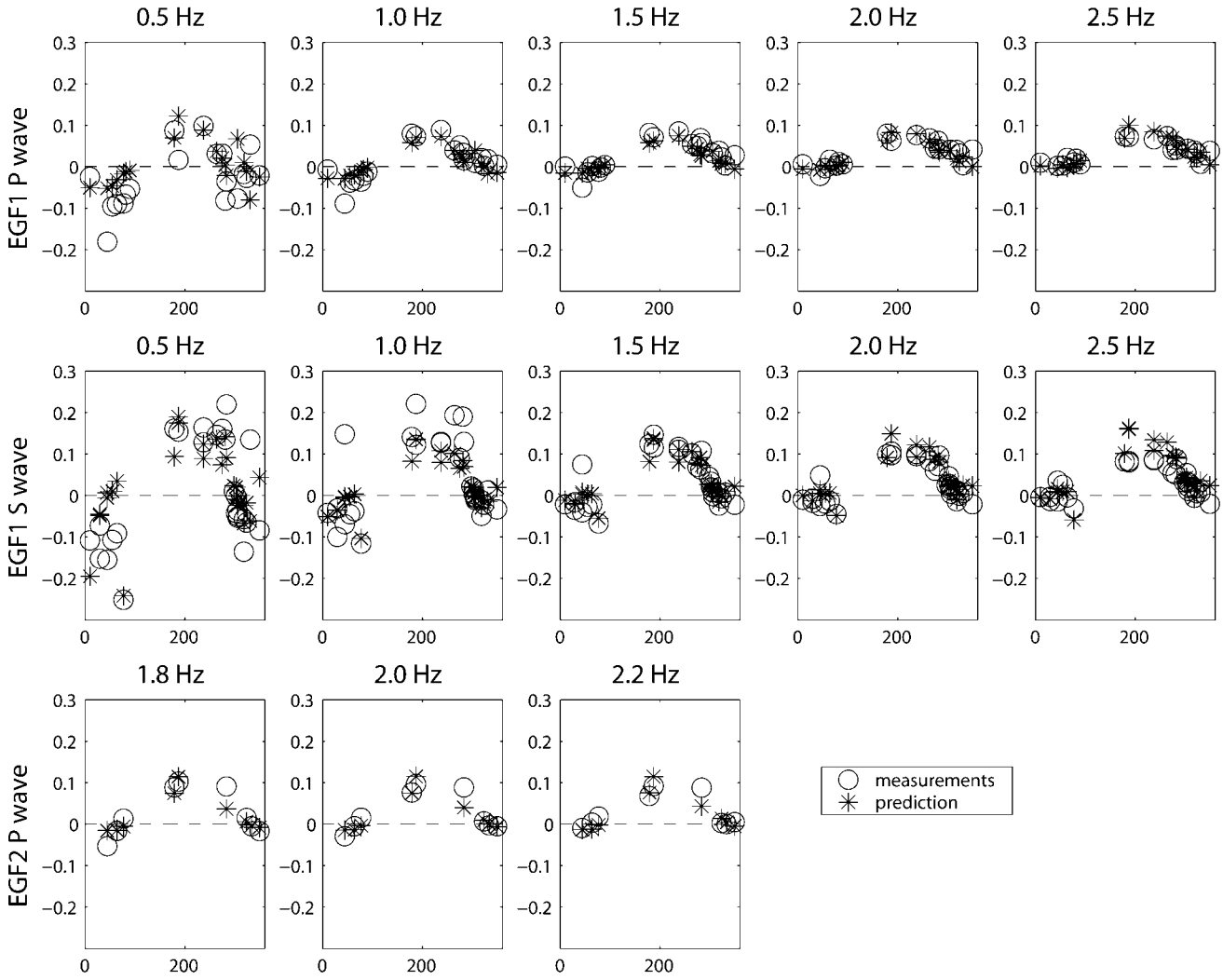

Figure 7. GSDF measurements of amplitude-reduction time as functions of azimuth and the fit of the inverted model. For EGF1, 19 *P* waves and 28 *S* waves were measured at frequencies ranging from 0.5 Hz to 2.5 Hz. For EGF2, 9 *P* waves were measured at frequencies of 1.8, 2.0, and 2.2 Hz. Circles, GSDF measurements; asterisks, predictions made with the inverted model and the sensitivity derivatives.

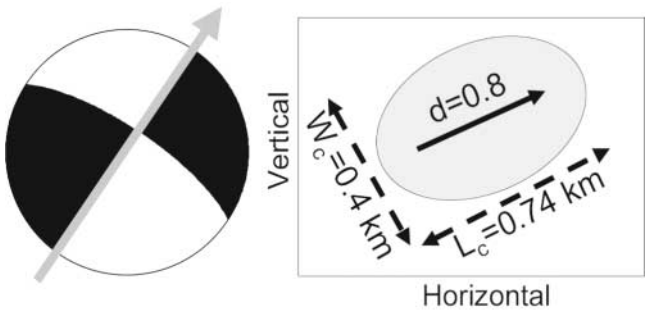

Figure 8. The inverted FMT parameters for the Yorba Linda event. (Left) The map view; arrow shows the orientation of the fault plane and directivity. (Right) The characteristic dimensions of the rupture; arrow shows the orientation of directivity.

2002), which shows an extension perpendicular to the Whittier fault (Fig. 9). It is also consistent with recent studies showing that a high proportion of the north–south shortening in the Los Angeles metropolitan region is accommodated by conjugate strike-slip faulting and east–west "escape" deformation (Walls *et al.*, 1998; Yeats, 2004).

To investigate the trade-offs among various source parameters, we sampled the solution space using a bootstrap method. The characteristic duration T_c is well constrained at 0.1–0.2 sec by the data, but we observed a strong trade-off between the characteristic length L_c and the directivity d (Fig. 10), which implies a large source (high L_c) has a low directivity, whereas a small source has a high directivity. Here we assume the rupture velocity, $v_R = L_c/[(2 - d)T_c]$, which ranges from $L_c/2T_c$ for a bilateral rupture ($d = 0$) to L_c/T_c for a unilateral rupture ($d = 1$). Another parameter of

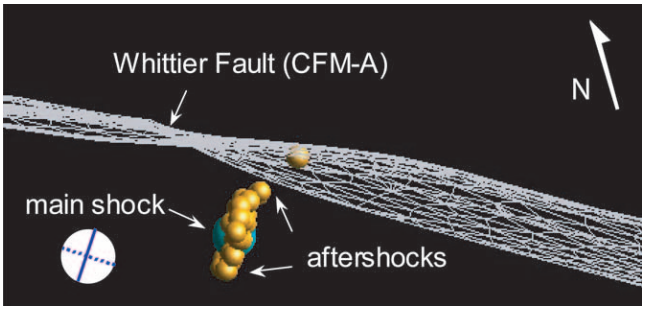

Figure 9. Projection of a 3D rendering of the Yorba Linda mainshock (blue sphere) and its aftershocks (gold sphere) relative to the Whittier fault (white triangulated surfaces). The relocated hypocenters were provided by E. Hauksson, the CFM-A model was provided by A. Plesch, and the 3D rendering using the LA3D visualization system was developed by the SCEC/Information Technology Research (ITR) interns.

concern is the stress drop. For L_c larger than 1.0 km, we obtain stress drop below 10 bars (first column on Table 1). If we require rupture velocity to be subshear (below shear-wave velocity) in our inversion, we obtain a more compact source with a higher stress drop of 32 bars and a directivity of 0.8 (second column on Table 1), and the fit to the observed data is equally good.

Many, if not most, large earthquakes display high directivity ($d > 0.5$), presumably owing to the heterogeneity of major faults (McGuire *et al.*, 2002). The results for the Yorba Linda earthquake contribute another datum in support of the notion that these symmetry-breaking processes also operate on a much smaller scale.

Conclusions

We have demonstrated that the FMT for a small earthquake can be recovered from regional waveform data. Our method is based on GSDF measurements of the differences between the observed and synthetic waveforms. Owing to the effects of 3D structure, we found it necessary to incorporate EGF-type constraints from aftershock data in the inversion of the differential amplitudes to resolve details of source finiteness. However, we note that even without using aftershock information, we were still able to determine the CMT solution and resolve fault-plane ambiguity by using synthetic Green's functions computed from path-specific 1D structure models. We have already adapted our method to use synthetics calculated from 3D models, such as the SCEC Community Velocity Model. FMT inversions using 3D synthetics for a set of earthquakes in the Los Angeles region will be presented in a subsequent article.

Our research suggests that improved versions of 3D models will eventually allow the automated recovery of FMTs for nearly all moderate earthquakes in well-instrumented regions like Southern California. When applied to a large number of events, this new technique should improve our understanding of regional tectonics and earthquake-scaling laws and provide new data for seismic-hazard analysis.

Acknowledgments

We thank Jeff McGuire for useful discussions and Egill Hauksson for his relocated aftershocks. Suggestions by Qinya Liu and an anonymous reviewer improved the article. This research was supported by the Southern California Earthquake Center (SCEC). SCEC is funded by National Science Foundation Cooperative Agreement EAR-0106924 and U.S. Geological Survey Cooperative Agreement 02HQAG0008. This article is SCEC contribution no. 810.

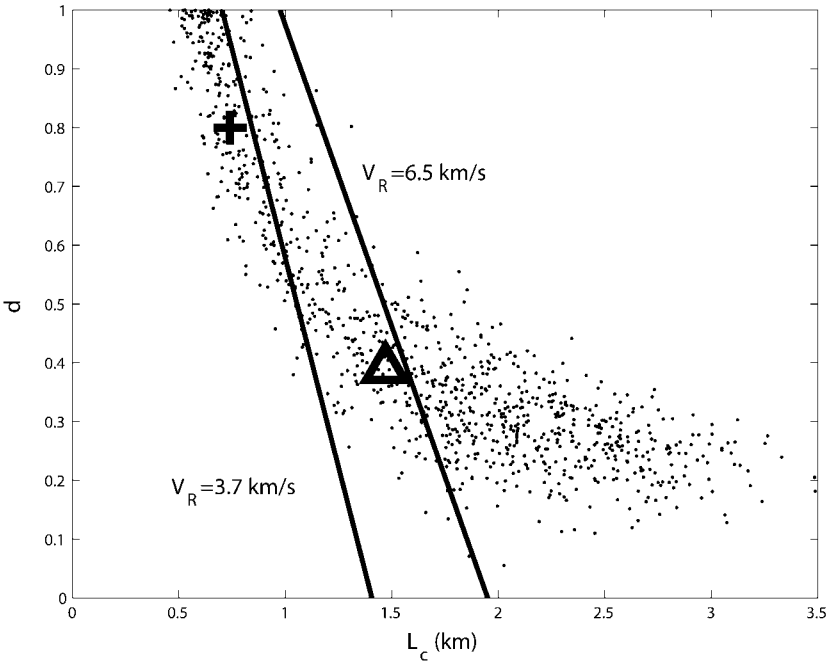

Figure 10. The solution space of the characteristic dimension L_c and directivity d as sampled by using a bootstrap method. The triangle shows the unconstrained solution (first column of Table 1), the plus shows the solution obtained under the subshear constraint (second column of Table 1). The two straight lines show constant rupture velocity at *P*- and S-wave velocity in the seismic-source region.

References

Backus, G., and M. Mulcahy (1976). Moment tensors and other phenomenological descriptions of seismic sources, I, Continuous displacements, *Geophys. J. R. Astr. Soc.* **46,** 341–361.

Ben-Menahem, A. (1961). Radiation of seismic surface-waves from moving sources, *Bull. Seism. Soc. Am.* **51,** 403–435.

Chen, P., L. Zhao, and T. H. Jordan (2003). A quantitative evaluation of SCEC community velocity model version 3.0 (abstract), *EOS Trans. AGU* **84,** no. 46 (Fall Meet. Suppl), S42H-02 (F1108).

Cohee, B., and G. Beroza (1994). Slip distribution of the 1992 Landers earthquake and its implications for earthquake source mechanics, *Bull. Seism. Soc. Am.* **84,** 692–712.

Courboulex, F., A. Deschamps, M. Cattaneo, F. Costi, J. Deverchere, J. Virieux, P. Augliera, V. Lanza, and D. Spallarossa (1998). Source study and tectonic implications of the 1995 Ventimiglia (border of Italy and France) earthquake (M_L = 4.7), *Tectonophysics* **290,** 245–257.

Dreger, D., and A. Kaverina (2000). Seismic remote sensing for the earthquake source process and near-source strong shaking: a case study of the October 16, 1999 Hector Mine earthquake, *Geophys. Res. Lett.* **27,** 1941–1944.

Dziewonski, A. M., T. A. Chou, and J. H. Woodhouse (1981). Determination of earthquake source parameters from waveform data for studies of global and regional seismicity, *J. Geophys. Res.* **86,** 2825–2852.

Gee, L. S., and T. H. Jordan (1992). Generalized seismological data functionals, *Geophys. J. Int.* **111,** 363–390.

Hauksson, E. (2000). Crustal structure and seismicity distribution adjacent to the Pacific and North America plate boundary in southern California, *J. Geophys. Res.* **105,** 13,875–13,903.

Hauksson, E., K. Hutton, L. Jones, and D. Given (2002). The M4.8 Yorba Linda, Orange County earthquake of 3 September 2002: California Integrated Seismic Network Preliminary Report, 2 pp.

Hauksson, E., P. Small, K. Hafner, R. Busby, R. Clayton, J. Goltz, T. Heaton, K. Hutton, H. Kanamori, J. Polet, D. Given, L. M. Jones, and D. Wald (2001). Caltech/USGS element of TriNet 1997-2001, *Seism. Res. Lett.* **72,** 690–704.

Hellweg, M., and J. Boatwright (1999). Mapping the rupture process of moderate earthquakes by inverting accelerograms, *J. Geophys. Res.* **104,** 7319–7328.

Jordan, T. H., and K. A. Sverdrup (1981). Teleseismic location techniques and their application to earthquake clusters in the south-central Pacific, *Bull. Seism. Soc. Am.* **71,** 1105–1130.

Komatitsch, D., Q. Liu, J. Tromp, P. Süss, C. Stidham, and J. H. Shaw (2004). Simulations of ground motion in the Los Angeles basin based upon spectral-element method, *Bull. Seism. Soc. Am.* **94,** 187–206.

Kohler, M. D., H. Magistrale, and R. W. Clayton (2003). Mantle heterogeneities and the SCEC reference three-dimensional seismic velocity model version 3, *Bull. Seism. Soc. Am.* **93,** 757–774.

Magistrale, H., S. Day, R. W. Clayton, and R. Graves (2000). The SCEC southern California reference 3D seismic velocity model Version 2, *Bull. Seism. Soc. Am.* **90,** no. 6B, S65–S76.

McGuire, J. (2004). Estimating finite source properties of small earthquake ruptures, *Bull. Seism. Soc. Am.* **94,** no. 2, 377–393.

McGuire, J. J., L. Zhao, and T. H. Jordan (2001). Teleseismic inversion for the second-degree moments of earthquakes, *Geophys. J. Int.* **145,** 661–678.

McGuire, J. J., L. Zhao, and T. H. Jordan (2002). Predominance of unilateral rupture for a global catalog of earthquakes. *Bull. Seism. Soc. Am.* **92,** 3309–3317.

Mori, J. (1996). Rupture directivity and slip distribution of the M 4.3 foreshock to the 1992 Joshua Tree earthquake, Southern California, *Bull. Seism. Soc. Am.* **86,** 805–810.

Mori, J., and S. Hartzell (1990). Source inversion of the 1988 upland, California, earthquake: determination of a fault plane for a small event, *Bull. Seism. Soc. Am.* **80,** 507–518.

Mori, J., H. Kanamori, J. Davis, E. Hauksson, R. Clayton, T. Heaton, L. Jones, A. Shakal, and R. Porcella (1998). Major improvements in progress for southern California earthquake monitoring, *EOS* **79,** 217–221.

Okada, T., N. Umino, Y. Ito, T. Matsuzawa, A. Hasegawa, and M. Kamiyama (2001). Source processes of 15 September 1998 M5.0 Sendai, Northeastern Japan, earthquake and its M3.8 foreshock by waveform inversion, *Bull. Seism. Soc. Am.* **91,** 1607–1618.

Pasyanos, M. E., D. S. Dreger, and B. Romanowicz (1996). Towards real-time determination of regional moment tensors, *Bull. Seism. Soc. Am.* **86,** 1255–1269.

Press, W. H., S. A. Teukolsky, W. T. Vetterling, and B. R. Flannery (2001). *Numerical Recipes in Fortran 77: The Art of Scientific Computing*, Cambridge University Press, New York.

Silver, P., and T. H. Jordan (1983). Total-moment spectra of fourteen large earthquakes, *J. Geophys. Res.* **88,** 3273–3293.

Süss, M. P., and J. H. Shaw (2003). P-wave seismic velocity structure derived from sonic logs and industry reflection data in the Los Angeles basin, California, *J. Geophys. Res.* **108,** no. B3, 2170, ESE 13.

Vandenberghe, L., and S. Boyd (1996). Semidefinite programming, *SIAM Rev.* **38,** 49–95.

Wald, D. J., and T. H. Heaton (1994). Spatial and temporal distribution of slip for the 1992 Landers, California earthquake, *Bull. Seism. Soc. Am.* **84,** 668–691.

Wald, D. J., T. H. Heaton, and K. W. Hudnut (1996). The slip history of the 1994 Northridge, California, earthquake determined from strong ground motion, teleseismic, GPS, and leveling data, *Bull. Seism. Soc. Am.* **86,** S49–S70.

Walls, C., T. Rockwell, K. Mueller, Y. Bock, S. Williams, J. Pfanner, J. Dolan, and P. Fang (1998). Escape tectonics in the Los Angeles metropolitan region and implications for seismic risk, *Nature* **394,** 356–360.

Yeats, R. S. (2004). Tectonics of the San Gabriel Basin and surroundings, southern California, *Geol. Soc. Am. Bull.* **116,** no. 9/10, 1158–1182.

Zhao, L., and T. H. Jordan (1998). Sensitivity of frequency-dependent traveltimes to laterally heterogeneous, anisotropic Earth structure, *Geophys. J. Int.* **133,** 683–704.

Zhao, L., T. H. Jordan, and C. H. Chapman (2000). Three-dimensional Fréchet differential kernels for seismic delay times, *Geophys. J. Int.* **141,** 558–576.

Zhu, L., and D. Helmberger (1996). Advancement in source estimation techniques using broadband regional seismograms, *Bull. Seism. Soc. Am.* **86,** 1634–1641.

Zhu, L., and L. A. Rivera (2003). A note on the dynamic and static displacements from a point source in multilayered media, *Geophys. J. Int.* **148,** 619–627.

Department of Earth Sciences
University of Southern California
3651 University Avenue
Science Hall 117
Los Angeles, California 90089

Manuscript received 14 May 2004.